Electronic Supplementary Information

Charge Collection Enhancement by Incorporation of Gold-Silica Core-Shell Nanoparticles in P3HT:PCBM/ZnO Nanorod Array Hybrid Solar Cells

Ting-Chung Wang[a], Yen-Hsun Su[b], Yun-Kai Hung[c], Chen-Sheng Yeh[c], Li-Wen Huang[b], Widianta Gomulya[d], Lai-Hung Lai[d], Maria A. Loi[d], Jih-Sheng Yang[a] and Jih-Jen Wu*[a]

[a]Department of Chemical Engineering, National Cheng Kung University, Tainan 701, Taiwan

[b]Department of Materials Science and Engineering, National Cheng Kung University, Tainan 701, Taiwan

[c]Department of Chemistry, National Cheng Kung University, Tainan 701, Taiwan

[d]Zernike Institute for Advanced Materials, University of Groningen, Nijenborgh 4, Groningen, 9747 AG, The Netherlands

* Corresponding author. E-mail address: wujj@mail.ncku.edu.tw

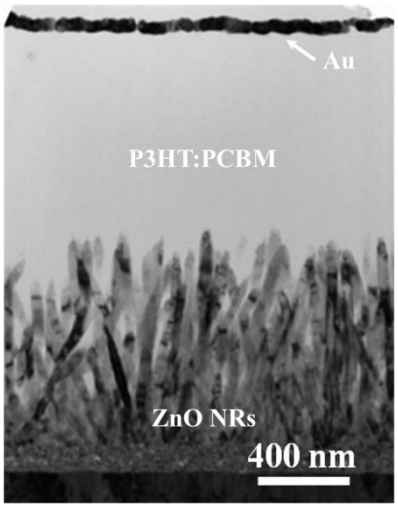

Figure S1 Cross-sectional TEM image of P3HT:PCBM/ZnO NR hybrid solar cell.

Formation of asymmetric quadrupole of Fano resonance on Au@Silica NP

The formation of the asymmetric quadrupole is mainly pertaining to the following reasons. As shown in Figure S2(a), the strong EM field of the surface plasmonic resonance of the Au-NP core (regions enclosed by the black dashed lines) induces an opposite dipole on the surface of the silica shell (regions enclosed by blue dashed lines). The LSPR-induced electric field on the surface of Au@Silica NP is therefore detracted by coupling with the opposite induced dipole. Moreover, the quadrupolar electric mode (regions enclosed by white dashed lines) is developed on the surface of the silica shell because of symmetry breaking by the ZnO NR and the continuous waves of the incident light. The quadrupolar electric mode coupling with the detracted LSPR on the surface of the silica shell leads to the asymmetric quadrupole on the surface of the Au@silica NP in the hybrid, as shown in Fig. 2(a).

The thickness of the silica shell of Au@silica-200 NPs is much thicker than that of Au@silica-50 NPs. As shown in Figure S2(b), the LSPR-induced electric field on the surface of Au@Silica NP is significantly detracted by coupling with the opposite induced dipole with increasing the thickness of the outer silica shell. Therefore, the dipole field of LSPR can not efficiently penetrate the silica shell, which results in the much weaker Fano resonance field in the P3HT:PCBM/ZnO NR hybrid (the outer part of the silica shell). The energy density distributions of Au@silica-50 NP and Au@silica-200 NP are thus different.

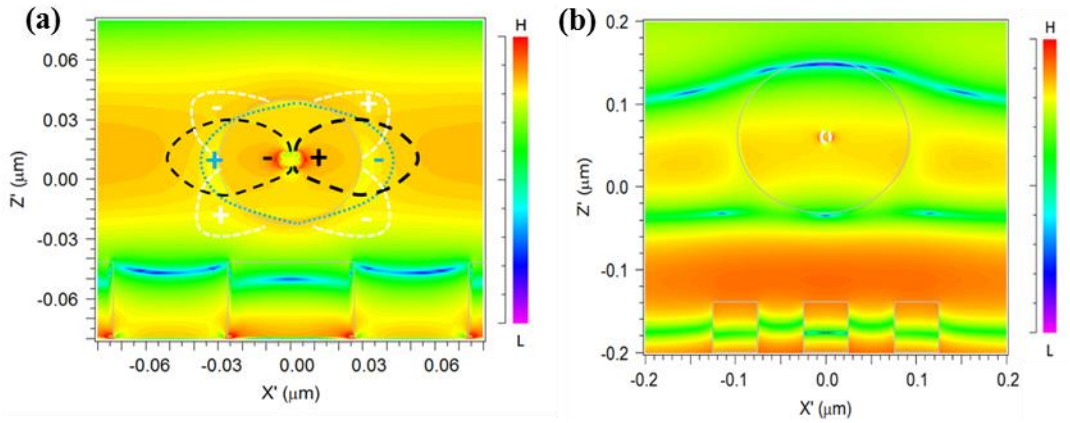

Figure S2 (a) Decomposition of simulated energy density distribution around Au@silica-50 NP in P3HT:PCBM hybrid with 530-nm continuous EM wave entering from ZnO NR array side. Regions enclosed by black dashed line: EM field of surface plasmonic resonance of Au-NP core; blue dashed line: opposite dipole on surface of silica shell induced by EM field of surface plasmonic resonance; white dashed line: quadrupole electric mode developed on surface of silica shell. (b) Simulated energy density distribution around Au@silica-200 NP in P3HT:PCBM active layer. Region enclosed by blue solid line is position of Au@silica NP.

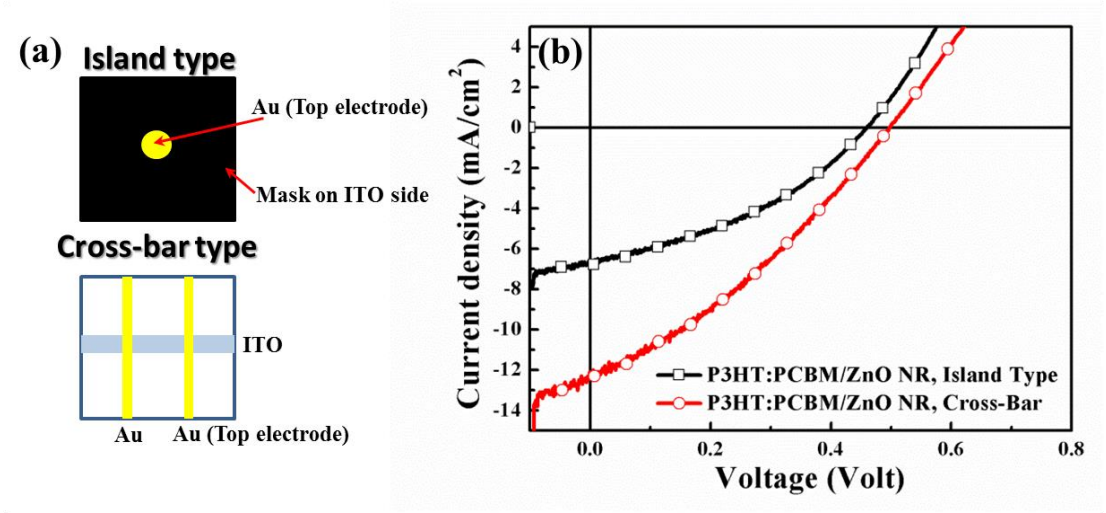

Figure S3 (a) Schematics of cross-bar-electrode and island-type electrodes. (b) J-V curves of P3HT:PCBM/ZnO NR hybrid solar cells with island-type-electrode and cross-bar-electrode configurations.

Table S1 Photovoltaic properties of P3HT:PCBM/ ZnO NR hybrid solar cells with island-type-electrode and cross-bar-electrode configurations.

	Voc (V)	**Jsc (mAcm^{-2})**	**FF**	**Efficiency (%)**
Island-type-electrode cell	0.46	6.63	0.38	1.17
Cross-bar-electrode cell	0.50	12.23	0.33	2.00

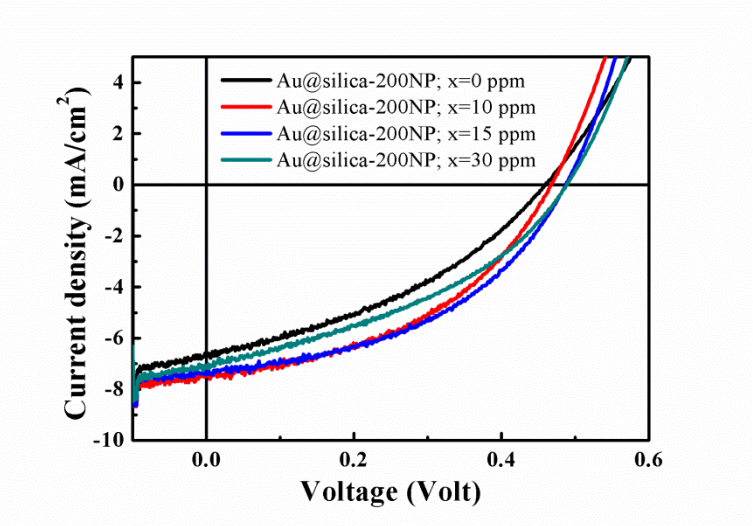

Figure S4 J-V curves of P3HT:PCBM/ZnO NR hybrid solar cells with various Au@silica-200 NP concentrations.

Table S2 Photovoltaic properties of P3HT:PCBM/Au@Silica NP/ZnO NR hybrid solar cells with various concentrations of Au@Silica-200 NPs in active layers.

	Voc (V)	**Jsc (mAcm^{-2})**	**FF**	**Efficiency (%)**
P3HT:PCBM/ZnO NR	0.46	6.63	0.38	1.17
With Au@Silica-200 NPs; *x*=10	0.47	7.48	0.44	1.54
With Au@Silica-200 NPs; *x*=15 (P3HT:PCBM/Au@Silica-200 NP/ZnO NR)	0.49	7.37	0.45	1.63
With Au@Silica-200 NPs; *x*=30	0.49	7.12	0.38	1.34

Statistical device parameters of P3HT:PCBM/ZnO NR, P3HT:PCBM/Au@Silica-50 NP/ZnO NR and P3HT:PCBM/Au@Silica-200 NP/ZnO NR hybrid solar cells

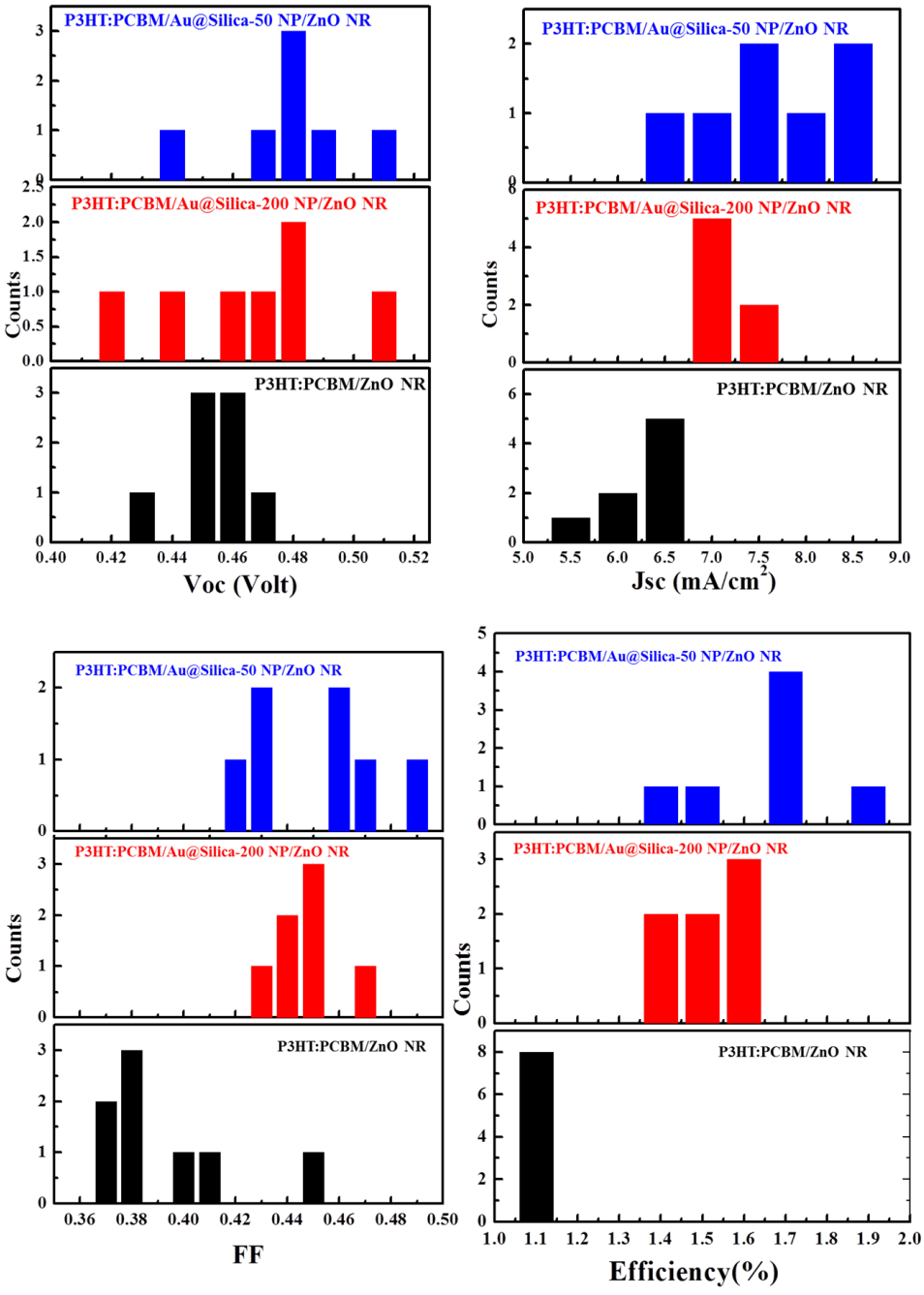

Figure S5 Histograms of device parameters (Voc, Jsc, FF, and η) for P3HT:PCBM/ZnO NR, P3HT:PCBM/Au@Silica-50 NP/ZnO NR and P3HT:PCBM/Au@Silica-200 NP/ZnO NR hybrid solar cells.

Table S3 Statistical device parameters of P3HT:PCBM/ZnO NR, P3HT:PCBM/Au@Silica-50 NP/ZnO NR and P3HT:PCBM/Au@Silica-200 NP/ZnO NR hybrid solar cells.

Hybrid solar cell		**Voc (V)**	**Jsc (mA/cm^2)**	**F.F.**	**η (%)**
P3HT:PCBM/ZnO NR	Avg.(3σ)	0.45 (0.04)	6.49 (1.42)	0.39 (0.08)	1.15 (0.06)
	Best η	0.46	6.63	0.38	1.17
P3HT:PCBM/Au@Silica-50 NP/ZnO NR	Avg.(3σ)	0.48 (0.06)	7.87 (1.86)	0.45 (0.08)	1.70 (0.4)
	Best η	0.48	8.03	0.49	1.91
P3HT:PCBM/Au@Silica-200 NP/ZnO NR	Avg.(3σ)	0.47 (0.09)	7.44 (0.76)	0.45 (0.04)	1.55 (0.24)
	Best η	0.49	7.37	0.45	1.63

Influences of Fano resonance on charge separation in P3HT:PCBM/ZnO NR hybrid

The energy potentials of the electron-hole pair state in P3HT as well as the electron and hole individually in P3HT and PCBM of the hybrid can be considered as harmonic potentials, as shown in Figure S3a. The crossing point of these two harmonic potentials is the activation threshold energy barrier for the electron-hole pair being separated to individual electron and hole in the hybrid. When an EC field is applied to the system, the two harmonic potentials will be perturbed by the field as $-\vec{p} \cdot \vec{E}$, where E is the applied electric field and p is the dipole. The corresponding Hamiltonian can be written as

$$H = H^0 - \vec{p} \cdot \vec{E} \qquad (1)$$

where H^0 is the original Hamiltonian and H is the Hamiltonian with the perturbation field. Therefore, the downward shifts of energy potentials are obtained in both pure P3HT and the P3HT:PCBM system, as illustrated in Figure S3a. Moreover:

$$\vec{p} = \varepsilon_0(\varepsilon_r - 1)\,\vec{E} \qquad (2)$$

where ε_0 and ε_r are the dielectric constant of vacuum and matter, respectively. Then:

$$H = H^0 - \vec{p} \cdot \vec{E} = H^0 - \varepsilon_0(\varepsilon_r - 1)\,\vec{E} \cdot \vec{E} = H^0 - \varepsilon_0(\varepsilon_r - 1)\,|\vec{E}|^2 \qquad (3)$$

At a wavelength of 530 nm (which produces the electric field of Fano resonance), the refractive index of P3HT is higher than that of the P3HT:PCBM hybrid.[1,2] The effective dielectric constant of the P3HT:PCBM system is therefore lower than that of pure P3HT. Using eq. (3), the downward shift of the energy potential of P3HT is deeper than that of the P3HT:PCBM system under the same electric field of Fano resonance, as represented by the solid lines in Figure S3a. Therefore, the activation threshold energy barrier of the electron-hole pair separation reaction is increased

when Fano resonance is triggered by the 530-nm-irradiated Au@silica NPs in the P3HT:PCBM/ZnO NR hybrid.

On the other hand, the refractive index of the ZnO:P3HT hybrid is higher than that of P3HT at 530 nm.[1] The activation threshold energy barrier is thus lower in the TiO_2 NR-ZnO NP/P3HT hybrid, as shown in Figure S3b, resulting from the higher dielectric constant of ZnO:P3HT compared to that of P3HT. The enhancement of charge separation by the electric field of the Fano resonance by the incorporation of Au@silica NPs is therefore achieved in the TiO_2 NR-ZnO NP/P3HT hybrid solar cells.[3]

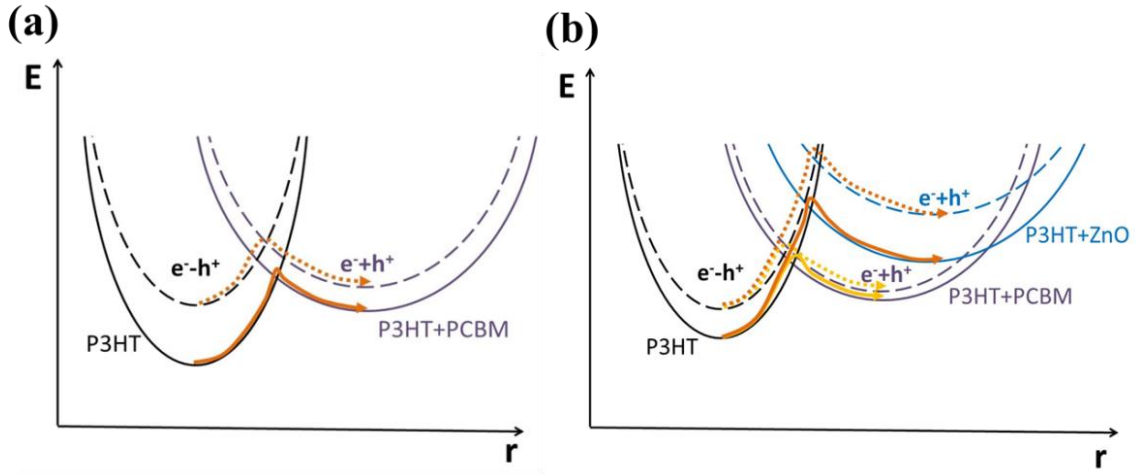

Figure S6 Energy potential diagrams of electron-hole pair states in (a) P3HT:PCBM system and (b) P3HT:PCBM and P3HT:ZnO systems. Dashed and solid lines are potentials without and with perturbed electric field, respectively. Black lines are potential of electron-hole pair. Purple lines are electron and hole under the separated condition. Orange lines are reaction paths.

References:

1. David E. Motaung, Gerald F. Malgas, Christopher J. Arendse, Sipho E. Mavundla, Materials Chemistry and Physics 135 (2012) 401-410
2. A.M.C. Ng, K.Y. Cheung, M.K. Fung, A.B. Djurišić, W.K. Chan, Thin Solid Films 517 (2008) 1047–1052.
3. W.P. Liao, Y.H. Su, Y.K. Huang, C.S. Yeh, L.W. Huang, J.J. Wu, ACS Appl. Mater. Interfaces 6 (2014) 17993−18000.